Title	Principal component analysis of observed and modeled diurnal rainfall in the maritime continent.
Author(s)	Teo, Chee Kiat.; Koh, Tieh Yong.; Lo, Jeff Chun Fung.; Bhatt, Bhuwan Chandra.
Citation	Teo, C. K., Koh, T. Y., Lo, J. C. F., & Bhatt, B. C. (2011). Principal Component Analysis of Observed and Modeled Diurnal Rainfall in the Maritime Continent . Journal of Climate, 24(17), 4662-4675.
Date	2011
URL	http://hdl.handle.net/10220/8222
Rights	© 2011 American Meteorological Society. This paper was published in Journal of Climate and is made available as an electronic reprint (preprint) with permission of American Meteorological Society. The paper can be found at the following official URL: [http://dx.doi.org/10.1175/2011JCLI4047.1]. One print or electronic copy may be made for personal use only. Systematic or multiple reproduction, distribution to multiple locations via electronic or other means, duplication of any material in this paper for a fee or for commercial purposes, or modification of the content of the paper is prohibited and is subject to penalties under law.

Principal Component Analysis of Observed and Modeled Diurnal Rainfall in the Maritime Continent

CHEE-KIAT TEO

Temasek Laboratories, Nanyang Technological University, Singapore

TIEH-YONG KOH

School of Physical and Mathematical Sciences, and Earth Observatory of Singapore, and Temasek Laboratories, Nanyang Technological University, Singapore

JEFF CHUN-FUNG LO AND BHUWAN CHANDRA BHATT

Temasek Laboratories, Nanyang Technological University, Singapore

ABSTRACT

Principal component analysis (PCA) is able to diagnose the diurnal rain cycle in the Maritime Continent into two modes that explain most of the diurnal variability in the region. The first mode results from the differential variation in potential instability forced by surface heat flux, insolation, and longwave radiative cooling on land and sea. The second mode is associated with intrinsic mesoscale dynamics of convective systems and its interactions with gravity waves, density currents, and local circulations in coastal regions or mountainous terrain. The spatial phase relation between the two modes determines whether a diurnal signal is propagating or stationary. Thus, validating model simulations of diurnal rainfall using PCA provides insights on the representation of dynamics and physics. In this paper, the main modes of diurnal rain variability in the Maritime Continent from satellite observations are studied and are compared with those from Weather Research and Forecasting (WRF) model simulations. Hovmoeller analyses of the reconstructed rainfall from the first two PCA modes clarify the impact of coastlines and mountains as sources of propagating signals. Wave cavities are identified in the Straits of Malacca, Malay Peninsula, and north Sumatra where stationary signals are produced. WRF reproduces the first two modes but each with a phase lead of about 1–2 h or longer, depending on the satellite rainfall product used for comparison. The basic diurnal forcing in the model seems to be too strong and the model responds too strongly to small islands and small-scale topography. The phase speed of propagating signals over open sea is correctly modeled but that over land is too slow.

1. Introduction

The Maritime Continent (MC) is often seen as the "boiler box" (Ramage 1968) whose latent heat release from precipitation is a significant energy source in driving the large-scale global atmospheric circulation. At the same time, the complex topography and coastline of the MC appear to have strong influence on the propagation of mesoscale convective complexes associated with the Madden–Julian oscillation (Neale and Slingo 2003; Hsu and Lee 2005; Shibagaki et al. 2006; Wu and Hsu 2009). Although the interactions of the region's weather systems across the spectrum of spatiotemporal scales are not well understood at present, the convective systems at diurnal time scales are very likely the basic components of the weather variability that rectify to the larger-scale weather variability in the tropics (Waliser and Moncrieff 2008).

Many studies reported shortcomings in reproducing the phase and amplitude of the diurnal cycle by regional (Clark et al. 2007; Koo and Hong 2010) and global atmospheric models (Neale and Slingo 2003; Dai 2006; Lee et al. 2007a,b; Qian 2008; Hara et al. 2009). The reasons may be related in part to boundary layer and convective parameterizations (Davis et al. 2003; Wang et al. 2007;

Koo and Hong 2010) and in part to inadequate grid resolution (Lee et al. 2007b; Sato et al. 2009). Such underestimation of precipitation as well as the phase shift of diurnal variability in the MC could lead to systematic errors in the latent and sensible heat fluxes in general circulation models (GCMs) (Neale and Slingo 2003; Qian 2008). Hence it is important to assess the model's ability to reproduce the diurnal weather variability in the MC and identify model deficiencies for accurate reproduction and prediction of present and future global climate, respectively. Similar effort will also benefit numerical weather prediction, especially for coastal cities where intense mesoscale storm systems that sometimes develop together with the diurnal sea breeze can result in flooding and significant economic losses (Wu et al. 2007).

The main aim of the paper is to demonstrate the usefulness of principal component analysis (PCA) (e.g., Jackson 1991) in assessing a mesoscale model's ability in reproducing the diurnal rainfall variability in the MC. PCA have been used to assess low-frequency atmospheric responses to the El Niño–Southern Oscillation in models (Renshaw et al. 1998; Peng et al. 2000; Wang et al. 2009), where the leading modes of variability and their principal component scores are compared with those from observations. This is the first time PCA is used to analyze model diurnal responses as a diagnostic on model physics.

Recently the fundamental modes of the variability of tropical diurnal rainfall from satellite observations have been investigated by Kikuchi and Wang (2008) using PCA. Their work reveals that the diurnal rain cycle over the global tropics can be represented with only two modes of variability: the first mode represents the overall temporal difference between the stationary rain peaks over land and seas and the second mode represents the propagating nocturnal rain peaks that are associated with complex topographies. In addition, the two modes are in time quadrature, a consequence of the significant contribution of the propagating diurnal rain features to the overall diurnal rain variability. Their work highlights the fact that the diurnal cycle in the tropics is highly regular in time and coherent in space, making PCA very suitable in representing the tropical diurnal cycle.

The strength of PCA to assess the model diurnal cycle comes from the fact that the mechanisms governing the two diurnal rain modes of variability are rather different: the first mode of diurnal rain cycle represents the stationary convective response of the inland and maritime atmosphere to surface sensible and latent heat flux, solar heating, and nocturnal longwave radiative cooling (Oki and Musiake 1994; Tao et al. 1996; Sui et al. 1997; Dai 2001). On the other hand, the land–sea breeze over

coastal land and sea, up- and downslope winds on elevated terrain, gravity waves, and gravity currents generated from deep convection are the likely mechanisms for the propagating rain features located in the MC (e.g., Yang and Slingo 2001; Mori et al. 2004; Zhou and Wang 2006; Wu et al. 2008, 2009a,b) and elsewhere (Yang and Slingo 2001; Mapes et al. 2003). The extent to which the modeled "stationary" and "propagating" modes of diurnal rain variability from PCA agree with the observed can serve as a diagnostic for the model's representation of convective and mesoscale dynamics and their interaction with surface processes.

2. Data and methodology

The observed rainfall data used in this study are the multisatellite rainfall estimates from the Tropical Rainfall Measuring Mission (TRMM) 3B42 version 6 (Huffman et al. 2007) for 2008. This dataset provides 3-hourly instantaneous rainfall rate at a horizontal resolution of $0.25° \times 0.25°$.

Half-hourly accumulated rainfall amount from the Weather Research and Forecasting model (WRF) (Skamarock et al. 2008) for the domain covering the MC (Fig. 1) for year 2008 is used in the study. The model is run at a spatial resolution of 25 km and 30 vertical levels with the model top at 50 hPa. Lateral boundary conditions are provided by the National Centers for Environmental Prediction (NCEP) final analysis (FNL) (available online at http://dss.ucar.edu). The Kain–Fritsch cumulus scheme (Kain and Fritsch 1990, 1993) and Yonsei University planetary boundary layer scheme (Noh et al. 2003) are used. Nudging of the WRF upper-level wind, temperature, and water vapor fields above the boundary layer toward the 6-hourly FNL winds is performed (Stauffer and Seaman 1990).

As both model and observed data are arranged in coordinated universal time (UTC), they are further processed to compensate for the temporal phase difference in the distribution of rain across the domain at any one instant of UTC due to the lead in the local solar time (LST) moving eastward. This is achieved at each location by 1) uniformly distributing accumulated WRF rainfall within a 30-min period of accumulation or linearly interpolating between 3-hourly 3B42 instantaneous rainfall, and 2) integrating from 0000 to 0300, 0300 to 0600, . . . , 2100 to 0000 LST. Finally, the rain amount for each LST interval is averaged for the entire year.

PCA is next applied to the 2008 average observed and modeled diurnal cycle of rainfall. The first two empirical orthogonal functions (EOFs) are used to reconstruct the diurnal cycle for the MC as a way to highlight the most important signals. The reconstructed rainfall across the
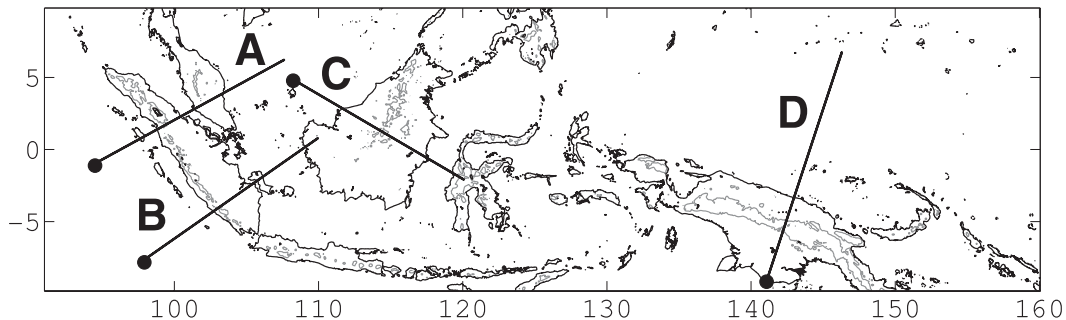
FIG. 1. The domain of interest for the present investigation. It encompasses the larger landmasses of the Maritime Continent, namely Sumatra, the Malay Peninsula, Borneo, and New Guinea. The four line sections A–D are focus regions where Hovmoeller plots of the diurnal rainfall are constructed (see text). The gray contours are terrain elevations at 1000 m.

focus regions (Fig. 1) is interpolated linearly at regular 1-km intervals along reference lines. Hovmoeller plots highlighting the propagation of the reconstructed rain peaks across the focus regions then allow the estimation of observed and modeled phase velocities. Appendix A shows that the correction in phase velocity arising from using LST instead of UTC is negligible.

Although the details of the region's diurnal cycle depend on the season (Oki and Musiake 1994), the gross diurnal rain features (~150 km in scale) over the MC are quite robust across seasons (Kikuchi and Wang 2008). Hence, the present investigations based on the annual average diurnal rain cycle would suffice to elucidate the main stationary and propagating modes of diurnal rain variability in the MC and to assess the capability of WRF in reproducing these two modes.

3. Diurnal cycle of rainfall

The observed and modeled diurnal cycles of rainfall (Fig. 2) show that WRF is able to capture the overall phase difference between sea and land with rainfall generally peaking in the evening on land and in the early morning over sea. But, over mountains, the rain starts too early and lasts too long in WRF. It is apparent that the modeled rain intensity is higher than the observed across most of the domain and especially over the mountains, with only a few exceptions, for example, southwest of the central ridge in New Guinea (Fig. 3). This difference could be model error or arise from observational undersampling: short-lived intense rainfall could be missed by 3B42's 3-hourly sampling period.

4. Principal component analysis

The first two EOFs and corresponding principal component scores (PCS) of the observed and modeled diurnal rainfall are shown in Figs. 4 and 5. The percentage variance of the diurnal cycle captured by the two EOFs

in the model and observations are similar: 93.3% and 90.9% respectively. The total variance in the model is 4.0 times that in the observations and, like the positive bias in the model mean, is due to overestimation of rainfall by WRF (Fig. 3).

EOF1 captures 1.7 times more variance than EOF2 and marks the fundamental phase difference between diurnal rainfall cycles over land and sea arising from the seesaw in the land–sea surface air temperature gradient. It basically represents the rise and fall of potential instability forced by the resultant of surface heat flux, insolation, and longwave radiative cooling during the day and night respectively, as PC1 shows. EOF1 also highlights a more intense diurnal cycle over high terrain compared to the surrounding lowland due to stronger solar forcing on the mountain slopes as well as valley breeze convergence toward the mountain ridges (Qian 2008).

EOF1 from WRF is similar to that from 3B42 but with stronger amplitude over the land and coastal sea. It also captures 3.4 times more variance than EOF2: this ratio is much higher than in the observations, implying that the basic diurnal forcing is too strong. Koo and Hong (2010) noted that, in the WRF model, the amplitude of the diurnal rain cycle is more sensitive to boundary layer parameterization over the East Asian landmass than over the ocean. Thus, the enhanced amplitude over land noted here is likely an overestimation by the model. PCA also reveals small-scale features that would not be easily detected otherwise; that is, the negative spatial loadings over land in southwest New Guinea and central eastern Borneo are smaller in extent and weaker in the model than in observations.

The positive spatial loadings of EOF2 in 3B42 denote nocturnal rain features as PC2 maximizes at night. The nocturnal inland rainfall in both Borneo and New Guinea is clearly highlighted. Rain peaks around Sumatra propagate away from the coastal ridge in western Sumatra toward the sea and inland as night falls (Mori et al. 2004;
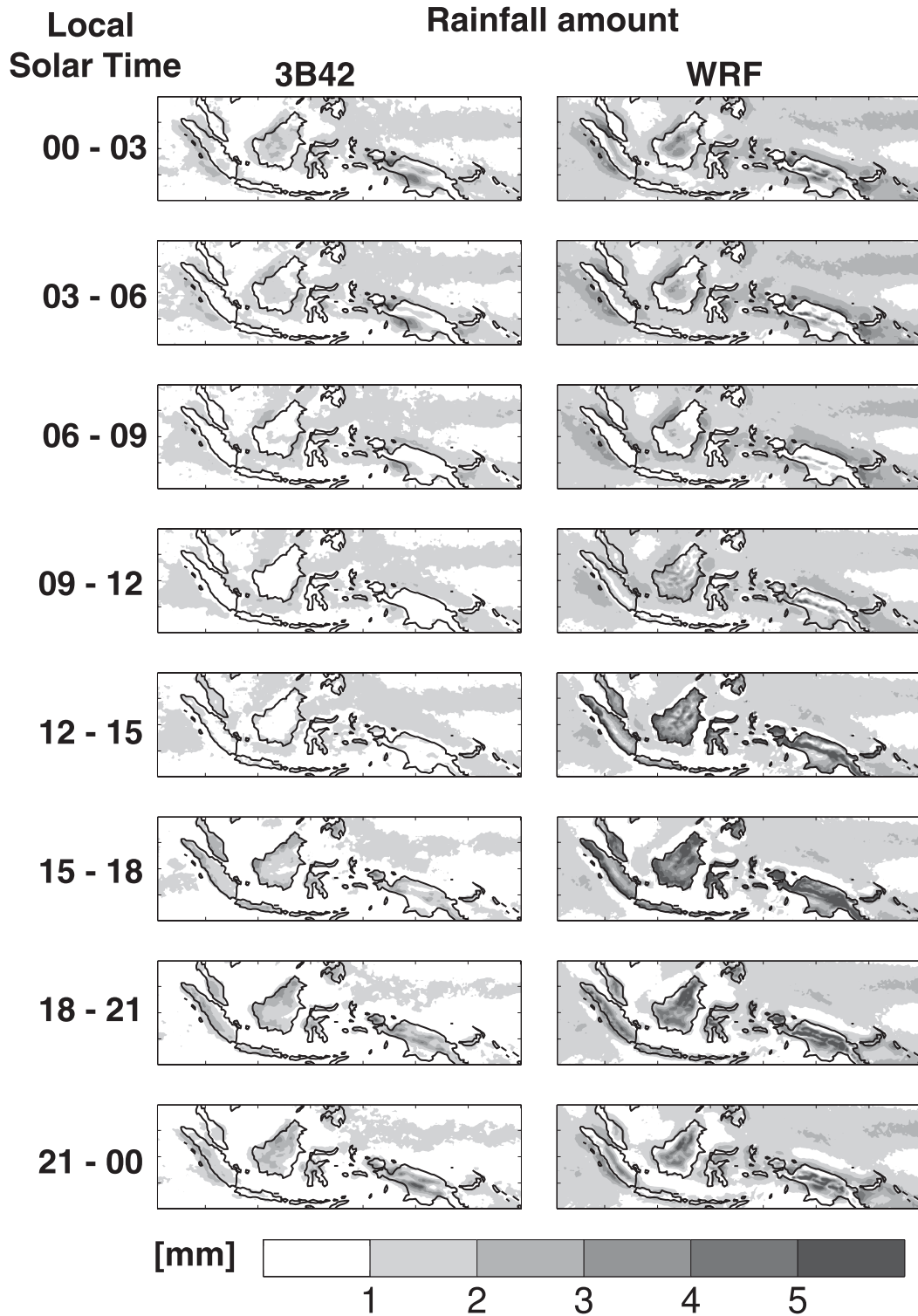
Local Solar Time

Rainfall amount

FIG. 2. All-season average 3-hourly accumulated rainfall in LST from WRF and 3B42 for the year 2008.
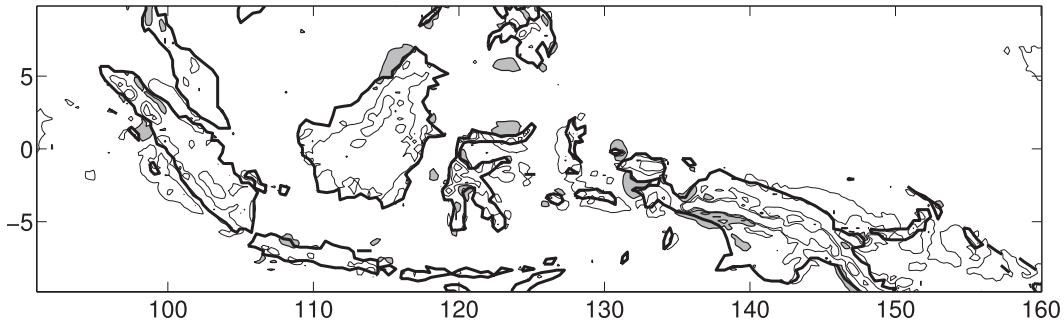
FIG. 3. The difference in the averaged 3-hourly accumulated rainfall between model and observation (model minus observed), Contour interval is 1 mm. Unshaded (shaded) contours are positive (negative) values.

Kikuchi and Wang 2008; Wu et al. 2009a). Similar seaward propagation of coastal rain along the northeastern coast of the Malay Peninsula, the western coast of Borneo, the eastern coast of Sulawesi and southward propagation of rain peaks from the mountain range of New Guinea into the southern plains can be seen.

EOF2 in the WRF model produces the above local diurnal rain features but with some differences upon detailed examination. Most notably, the spatial extent of the positive spatial loadings or nocturnal rain peaks in the plains east of the western ridge in western Sumatra and south of the central ridge of New Guinea, and in the coastal sea around Sulawesi, is less than the observed, reflecting slower propagation speed in the model. In fact, seaward from much of the northwestern Borneo coast positive spatial loadings are absent, indicating no effective propagation of the evening rain features from land into the coastal seas off the Borneo.
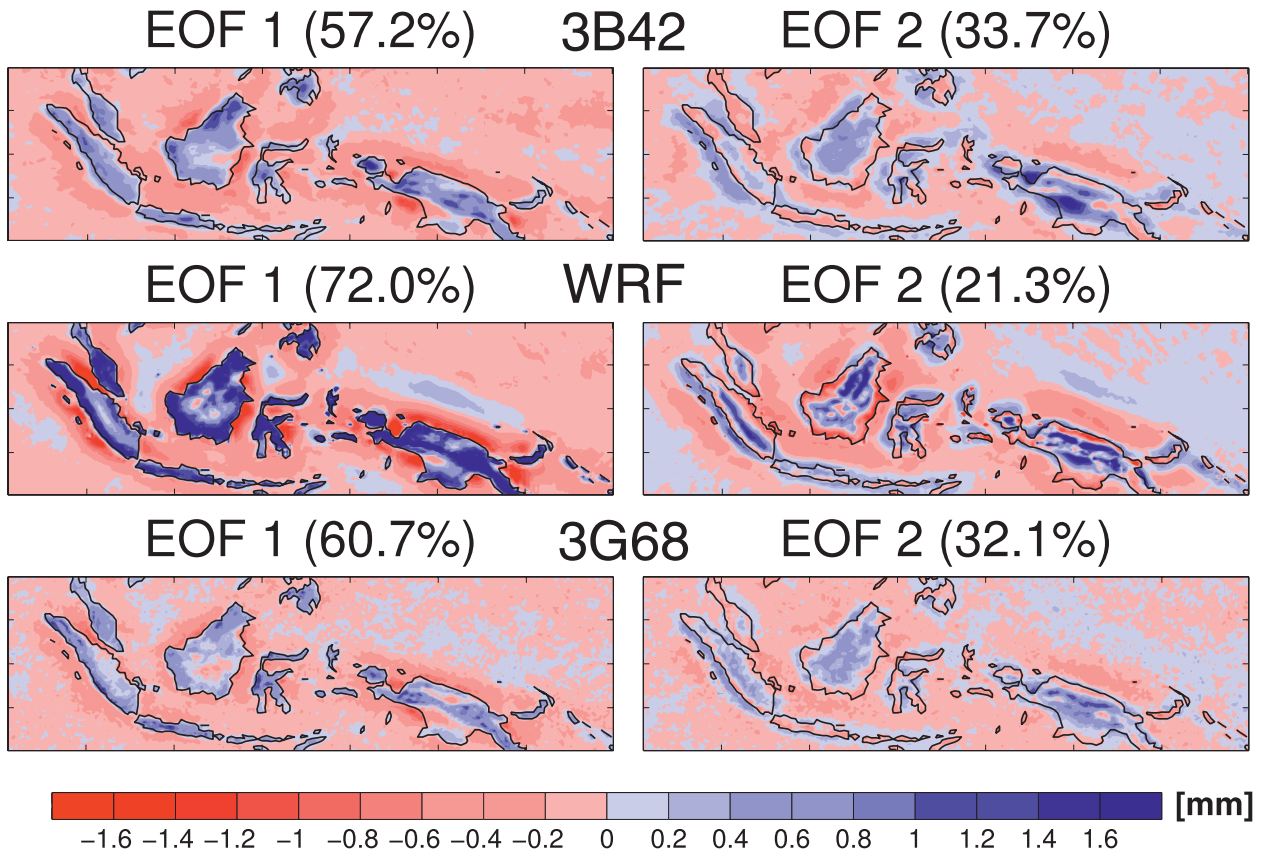

FIG. 4. The first two empirical orthogonal functions (EOFs) of the observed and modeled year-averaged diurnal rain cycle. The percentage of the total variability explained for each EOF is shown in the parentheses on top of each plot.
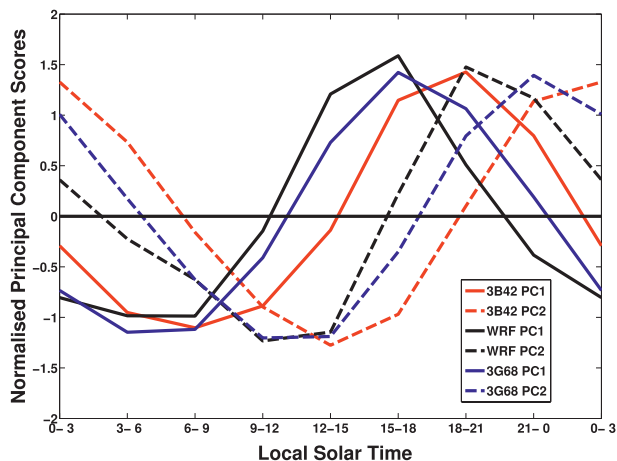
FIG. 5. The principal component scores corresponding to the EOFs in Fig. 4. Note that the PCS have been normalized to variance 1.

The model PC1 and PC2 both lead the observed by about 3 h. Similar findings have also been reported in several GCMs (Bechtold et al. 2004; Dai 2006; Lee et al. 2007a) and regional mesoscale models (Davis et al. 2003; Clark et al. 2007; Koo and Hong 2010). The phase of modeled diurnal rainfall is sensitive to the convective parameterization used. The more common shortcomings in convective schemes include too strong a relation between model convection with the convective available potential energy (CAPE) (Bechtold et al. 2004; Lee et al. 2007a), underrepresentation of cloud development (Guichard et al. 2004), and lateral entrainment/detrainment rates in deep and shallow convection (Wang et al. 2007). All of these deficiencies have the effect of moving forward the onset of deep convection (Guichard et al. 2004; Wang et al. 2007; Chaboureau et al. 2004).

5. Robustness to change in satellite dataset

A technical reason might also have contributed to the phase mismatch between the model and observed PCS. The 3B42 uses infrared (IR) sensing estimates, which have a stronger association with clouds than with precipitation. There have been reports that 3B42 rainfall estimates lag in situ gauge measurements (Zhou et al. 2008) and combined TRMM precipitation radar (PR) and TRMM Microwave Imager (TMI) rainfall estimates (Kikuchi and Wang 2008) by up to several hours, depending on location and time.

To investigate the last possibility, a further comparison with the diurnal rainfall computed from 12 years (1998–2009) of combined PR–TMI rainfall estimates (Haddad et al. 1997) in the TRMM 3G68 product was made at $0.25° \times 0.25°$ resolution (available online at

ftp://trmmopen.gsfc.nasa.gov/pub). Two provisos must be mentioned when using 3G68 data: 1) the sample size per 3-h interval for 3G68 is only about 45%–60% that of 3B42 and 2) PR and TMI estimates are still indirect measurements of rainfall rate.

First, the average rainfall was computed for half-hour intervals of a day (in LST) over the 12 years of 3G68 data. As this time series would suffer from variable sampling, as pointed out by Negri et al. (2002), a 3.5-h centered running mean was applied. (The results were also similar when a 4.5-h centered running mean was applied.) Finally, the rainfall was accumulated over 3-h intervals and PCA was performed on the diurnal cycle.

The 3G68 results confirmed that the main features in the 3B42 EOF1 and EOF2 are robust. One notable exception is that the patch of positive spatial loading in the coastal sea off north Borneo is much smaller in 3G68 EOF2 and hence in better agreement with the model (Fig. 4). The phase lead of the model rain from the observed rain can still be seen when using 3G68 PCS although the difference is reduced to about 1–2 h (cf. the zeros of the PCS in Fig. 5).

The remaining discussion focuses on the results for 3B42, as it has a larger sample size. Care was taken to leave out the occasional one or two features that are not robust between the two satellite datasets.

6. Hovmoeller analysis of reconstructed 3B42 rainfall

Figure 6 demonstrates the diurnal cycle in the MC diagnosed from 3B42 as the superposition of stationary and propagating signals. Whether the signal at a location is stationary or propagating can be understood from the relative phase of EOF1 and EOF2 at that location. Appendix B outlines how the spatial phase difference between the EOFs can give rise to stationary and propagating signals. Where the two EOFs are in quadrature, the resultant rain signal is propagating. Examples are the observed seaward propagation from the coasts of the east Malay Peninsula (section A in Fig. 6), west Sumatra (sections A and B), west Borneo (section B), and north New Guinea (section D), and simultaneous northward and southward propagation from the central mountain ridge in New Guinea (section D). Closer examination of Fig. 6 also reveals westward (eastward/northward/southward) propagation when the local EOF2 pattern is displaced westward (eastward/northward/southward) from the local EOF1 pattern while PC2 lags behind PC1 in time (Fig. 5). When the local patterns in the two EOFs are in phase or antiphase, the diurnal signal is stationary, such as observed on the Malay Peninsula, Straits of Malacca, north Sumatra
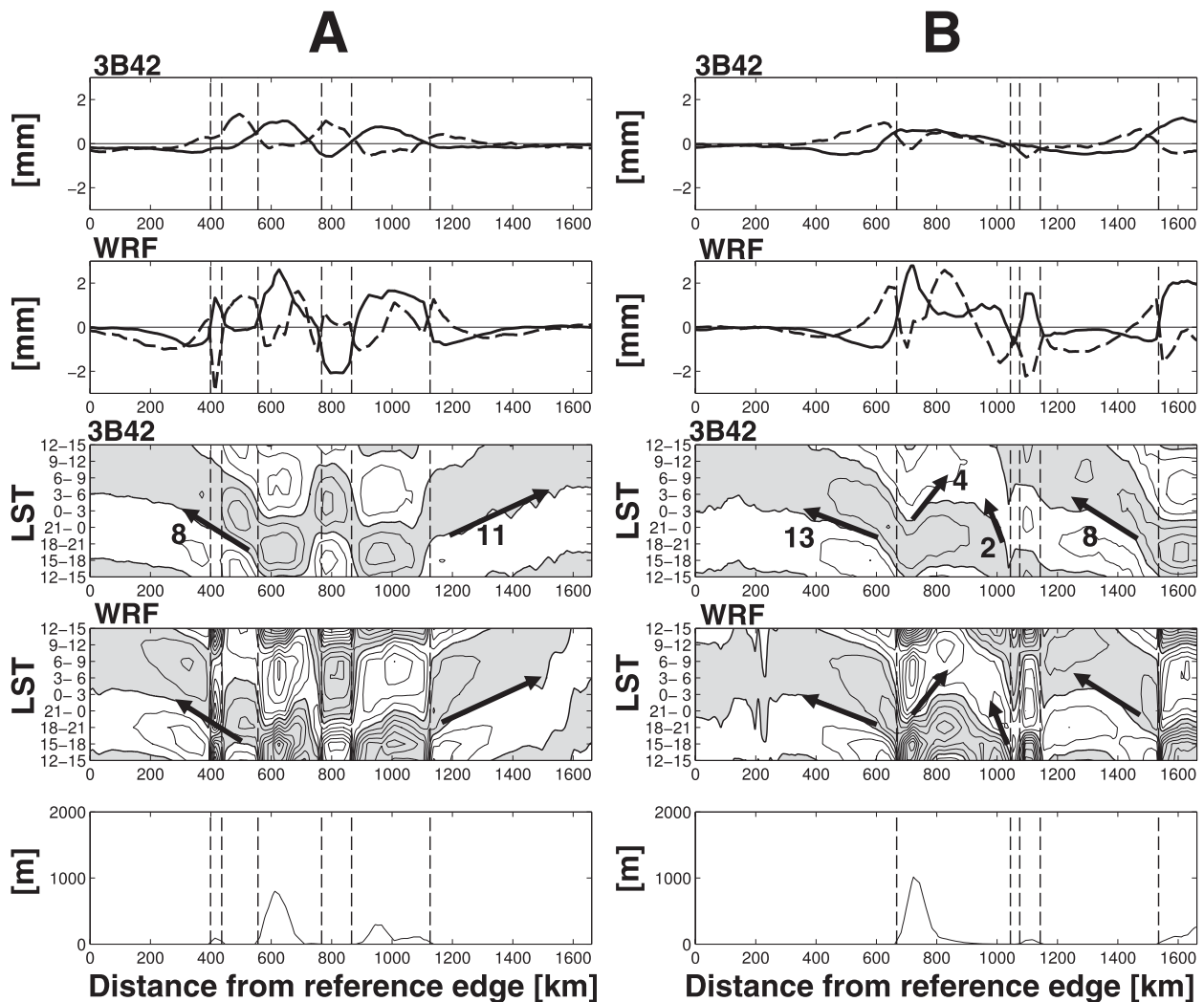
FIG. 6. (top two rows) EOFs and (next two rows) Hovmoeller analyses of reconstructed rainfall diurnal cycle from 3B42 and WRF along sections A, B, C, and D in Fig. 1. Distance along the lines is measured from the ends with the heavy dots in Fig. 1. The modeled terrain height is shown in the last row. In the top two rows, solid and dashed lines denote EOF1 and EOF2, respectively. In the next two rows, positive (negative) contours are shaded (unshaded) with a contour interval of 0.5 mm. The arrows and associated numbers (m s^{-1}) in the third row mark the estimated phase speed from 3B42 data. The arrows are duplicated in the fourth row for comparison with WRF results. Vertical dashed lines demarcate land–sea boundaries in the model.

(section A), and inland Borneo (section C). The spatially varying phase relation between EOF1 and EOF2 over MC that gives rise to a combination of propagating and stationary signals can be discerned by careful inspection of the zero contours in Fig. 4.

a. Sources of propagating diurnal signals

It is clear from Fig. 6 that the mountain ridges and coastlines in the MC are dominant sources of propagating rain signals. These propagating signals in the year-averaged diurnal cycle are likely the combined result of several different physical mechanisms explained below.

Rain often develops on mountain slopes during the late afternoon owing to convective instability induced by elevated heating of air by the mountain. The rain can migrate downslope in the early evening with a self-replicating mechanism involving cold pool dynamics under the influence of downslope mountain winds (Zhou and Wang 2006; Ichikawa and Yasunari 2006, 2008; Hara et al. 2009).

Over the coastal sea, a strong offshore wind can develop during the evening from slope winds redirected offshore at the base of coastal mountains (Wu et al. 2009b) or from the dynamical response to the formation of a steep temperature gradient across the land–sea boundary as a result of evening precipitation over the coastal land (Wu et al. 2008). The offshore winds can trigger convection over the coastal seas, and subsequently
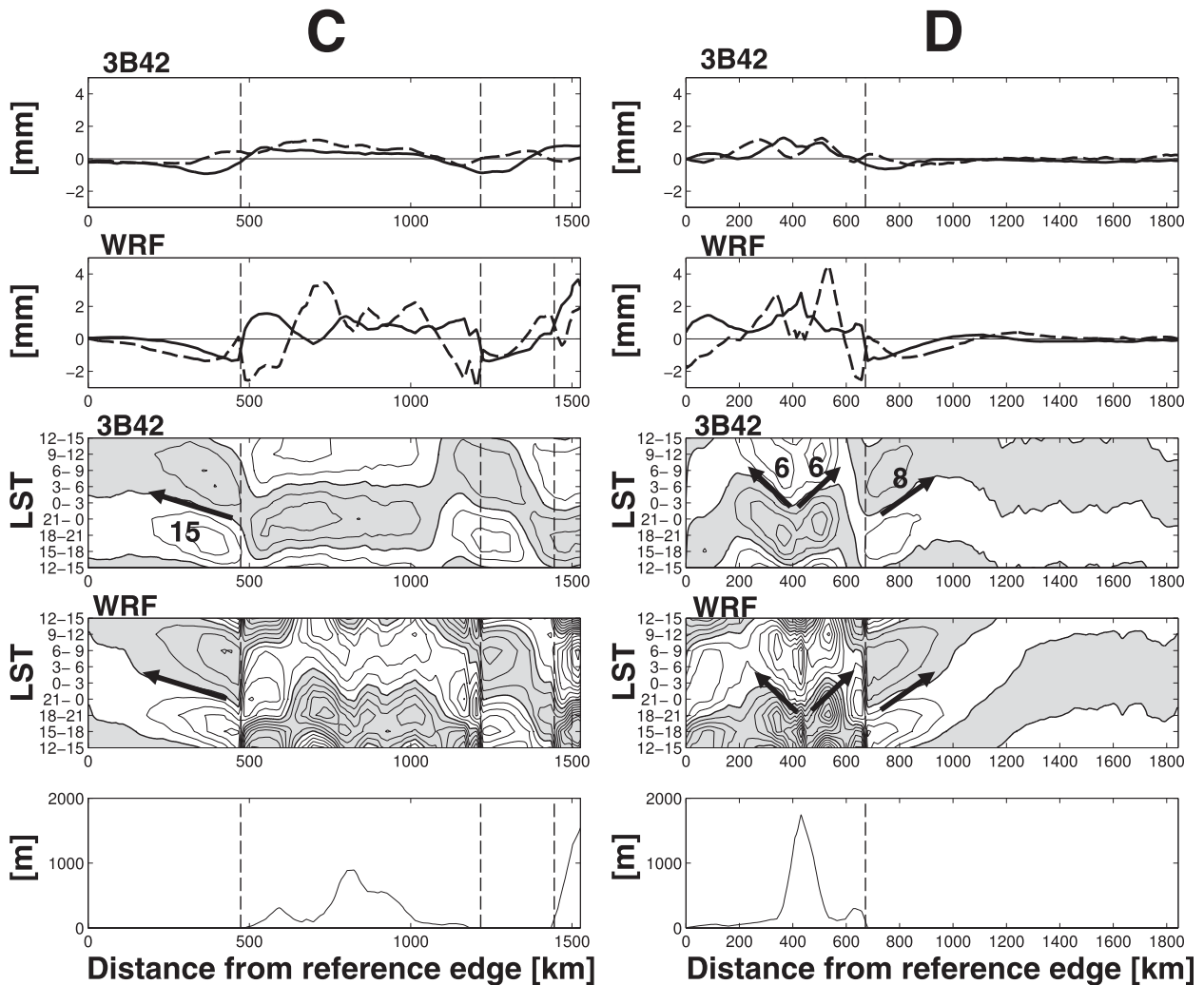
FIG. 6. (*Continued*)

these convective systems can propagate by means of gravity wave excitation from the latent heating profiles of antecedent convective cells (Mori et al. 2004; Ichikawa and Yasunari 2006) or through self-replication at the leading edge of a gravity current formed from convective downdraft in a similar way to squall propagation (Wu et al. 2009b). Some studies also suggested that, in the vicinity of coastal mountains, the diurnal oscillation of the elevated boundary layer over the mountains excites seaward-propagating gravity waves, which can destabilize the offshore air columns and trigger deep convection (Mori et al. 2004; Zhou and Wang 2006; Ichikawa and Yasunari 2008).

b. Impact on the local diurnal cycle

The impact of the surrounding geography on the local diurnal rain cycle in the MC can be understood readily using the concept of coastlines and mountains as sources of propagating signals. For example, the local diurnal rain cycles of islands off west (section A in Fig. 6) and east (section B) Sumatra are not apparent in the 3B42 Hovmoeller plots because they have been overwhelmed by propagating signals from the west Sumatra coast and the west Borneo coast, respectively.

The Hovmoeller plot for section C in Fig. 6 suggests that the observed westward propagating signal from the coastline in west Sulawesi extends into the eastern coastal plain of Borneo. This signal almost completely reverses the phase of the diurnal cycle over east Borneo relative to the rest of island (cf. also 3B42 EOF1 in Fig. 4). Indeed, westward-propagating diurnal gravity waves excited from convection over the mountains in Sulawesi were found to suppress evening convection over east Borneo (Wu et al. 2009a).

c. Formation of stationary diurnal signals

The Straits of Malacca together with the adjacent east Sumatra coast and west Malay Peninsula coast (section A in Fig. 6) can be thought as geophysical fluid dynamical (GFD) analogs of a wave cavity. In this case, an eastward-propagating signal from the east coast of Sumatra interferes with a westward propagating signal from the west coast of Malay Peninsula and results in the formation of a stationary signal over the Straits of Malacca as illustrated in the schematics in Fig. 7a. The idea of the straits and the adjacent coastal lands forming a coupled dynamical system is supported by recent numerical simulations. Fujita et al. (2010) suggested that the convergence of offshore winds driven by gravity currents from evaporative cooling of precipitation over the eastern and western coastal land of Sumatra and Malay Peninsula respectively can be an important triggering mechanism for convection over the straits.

In the same way, north Sumatra and the Malay Peninsula may each be understood as wave cavities trapped between their own western and eastern coastlines, thus manifesting stationary diurnal signals (section A in Fig. 6) as depicted in Fig. 7a. Such convergence of propagating signals from coastlines over land was reported by Joseph et al. (2008) in a numerical simulation where the triggering of convection over the southern Malay Peninsula can occur as a result of collusion of sea-breeze fronts propagating from the eastern and western coasts. For the counterpropagating signals from the two ends to interfere, the GFD wave cavity (i.e., the straits, peninsula, or long island) must not be too wide. Otherwise, signals from each end would not propagate all the way to the other end due to attenuation. In that case, the central portion of the cavity manifesting the stationary interference signal is expected to slowly shrink with increasing cavity width (Fig. 7b). This is indeed the case observed in south Sumatra island (section B, Fig. 6) where the coast-to-coast separation is about 80% wider than in north Sumatra island (section A).

d. Observed phase speeds

The estimated phase speeds for the observed propagating rain signals are estimated to be 8–15 m s^{-1} over open sea and 4–6 m s^{-1} over land (down mountain slopes and across open plains). These values are comparable with phase speeds of propagating rain features in the MC estimated from observations and numerical experiments reported elsewhere (Mori et al. 2004; Ichikawa and Yasunari 2008; Wu et al. 2009b). Our phase speed estimates suggest that the propagating signals are slower over land than over open sea. Such difference is also observed by Ichikawa and Yasunari (2008). Propagating

rain signals over sea associated with gravity wave activity are likely to travel faster than propagating rain signals over land under the density current mechanism (Mapes et al. 2003). As for rain signals propagating over sea by the density current mechanism, the phase speed could still be faster than over land due to lower surface roughness impeding the advance of the cold pool (Hatcher et al. 2000). Another reason may be that the lower roughness over the sea induces weaker surface heat fluxes, so the temperature and hence density contrast between the gravity current and the ambient air is better maintained, leading to greater propagation speed (Ross et al. 2004).

7. Hovmoeller analysis of reconstructed WRF rainfall

The general phase lead of the modeled diurnal cycle can be seen from Fig. 6. This is consistent with the modeled PCS leading observed PCS in Fig. 5 and so needs no further comment.

The model responds too strongly to small islands, giving rise to spurious high wavenumber components in the model EOFs. The propagating signals across the islands west of north Sumatra and east of south Sumatra are overwhelmed by local stationary signals, resulting in a "landlike" diurnal phase (sections A and B in Fig. 6, respectively). EOF1 and EOF2 also vary too much with small-scale topographic features. This causes the unrealistic aggregations of modeled rainfall at scales of 120–150 km over inland Malay Peninsula, Sumatra, Borneo, and New Guinea, confusing the otherwise clear stationary diurnal signal. A repeat of the model experiment with smoothed topography greatly reduces these unrealistic features and confirms that small-scale topography is the main cause for the excitation of higher wavenumbers in the model EOFs (Fig. 8). One plausible reason for the absence of such sensitivity to small-scale terrain or island features in the observations may be that subgrid-scale irregularities in the actual terrain or coastline destroy the coherence of small-scale propagating signals, which then do not contribute to the year-averaged diurnal cycle.

In the model, the strip of sea between the west of the north Sumatra coast and its offshore island chain appears to constitute a GFD wave cavity (section A in Fig. 6) similar in principle to that of the Straits of Malacca. Since the two bodies of water are almost equally wide, it is unlikely that 3B42 measurements have missed the stationary signal in one but not the other. The stationary diurnal signal immediately west of Sumatra is likely to be an artifact due to wave trapping by the offshore island chain in the model. A similar but less severe trapping is seen in the wider sea between west Borneo and the offshore island east of Sumatra
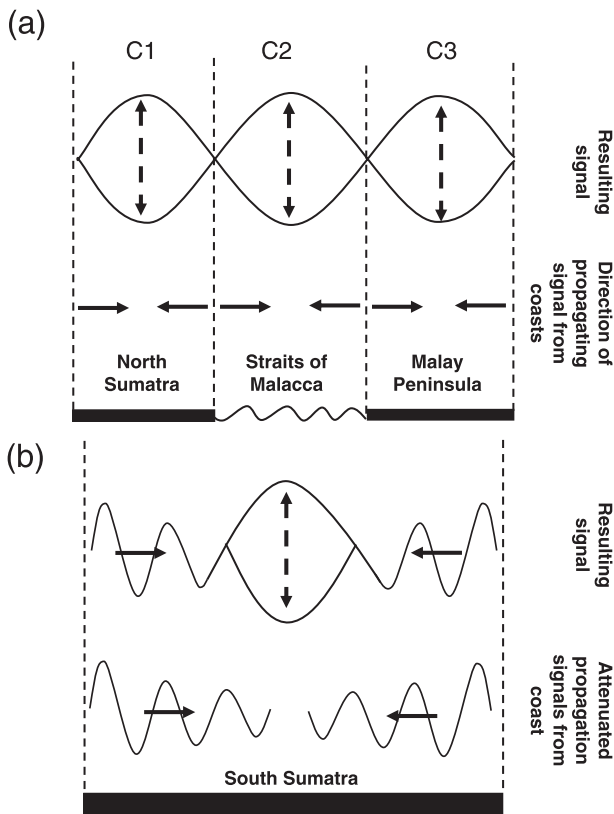
(a)

(b)

FIG. 7. Schematic of interference of trapped waves in wave cavities. (a) Interference of waves from the coast resulting in a stationary signals over the three cavities C1, C2, C3 over north Sumatra, the Straits of Malacca, and the Malay Peninsula, respectively. (b) Over south Sumatra, attenuation of the propagating signal resulted in a smaller standing-wave signal with respect to the cavity width. Propagating signals are still dominant around the coastal regions.

(section B), where the spurious counterpropagating wave from the island east of Sumatra does not penetrate all the way back to west Borneo owing to attenuation.

Over land, WRF reproduces the propagating rain signals with somewhat slower phase speed to the observed, downslope from the mountain ridges in New Guinea (section D in Fig. 6). The modeled signal does not migrate as far south over the plains from the ridge in New Guinea as noted in the observations. The rain propagation over open sea is well captured with the correct phase speed in all instances. But the signals migrate too far north into the Pacific Ocean from the north coast of New Guinea (section D). Thus, the rain features may be too strongly attenuated on land but too weakly attenuated over sea in the model.

The overattenuation of propagating signals over land may be symptomatic, in part, of the limitation of cumulus parameterization schemes in representing cold pool dynamics and the interaction between convection and the

local circulation reported in several investigations in the MC (Hara et al. 2009) and elsewhere (e.g., Davis et al. 2003; Clark et al. 2007). Models that explicitly resolve convection have been shown to be able to simulate correctly the propagation of mesoscale rain systems in the MC (Hara et al. 2009; Sato et al. 2009).

Certain modeled rain signals do not propagate smoothly across the coastline from land to sea. For example, the diurnal rain signal in the Straits of Malacca is broken from the adjacent signals in coastal Sumatra and the Malay Peninsula (section A in Fig. 6), and likewise for west Borneo (section B). Instead, the coastal land and sea diurnal signals seem to be in antiphase. This problem is evident from the sharp transition of the EOFs across the coastlines and may perhaps be related to the lack of subgrid-scale irregularities in the coastlines, which would have provided a smoother transition from land to sea at grid scale. Another reason could be that, as seen in some model simulations (Qian et al. 2003), the discontinuity in model surface parameterization between land and sea causes an abrupt change in the atmospheric boundary layer and interferes with the smooth propagation of gravity currents and gravity waves across the land–sea boundary.

8. Conclusions

Principal component analysis is shown to provide a compact description of the diurnal cycle for the MC, allowing straightforward comparison between observed and modeled diurnal rain variability. The diurnal rain features in the observations and model are encapsulated within the first two EOFs, the PCS of which are in time quadrature. The two EOFs are physically based modes. The first EOF is strong and represents the fundamental atmospheric response to potential instability forced by radiation and surface heat flux over land and sea during day and night, respectively. The positive loadings of the second EOF by itself represent the local nocturnal rain features downslope of elevated terrain (e.g., in Sumatra and New Guinea), over coastal land and sea, or inland of the large island of Borneo, resulting from the interaction between mesoscale convection and gravity waves, density currents, or local thermally induced circulations.

The differences in the dynamics behind the two EOFs can give insight as to where the model represents well and where it falls short. The first EOF of the WRF model is similar to the observed but has larger amplitude over land, particularly over elevated terrain, which is likely due to deficiencies in the boundary layer parameterization. It also captures too much variance over the second EOF, implying that the basic diurnal forcing is too strong in the model.
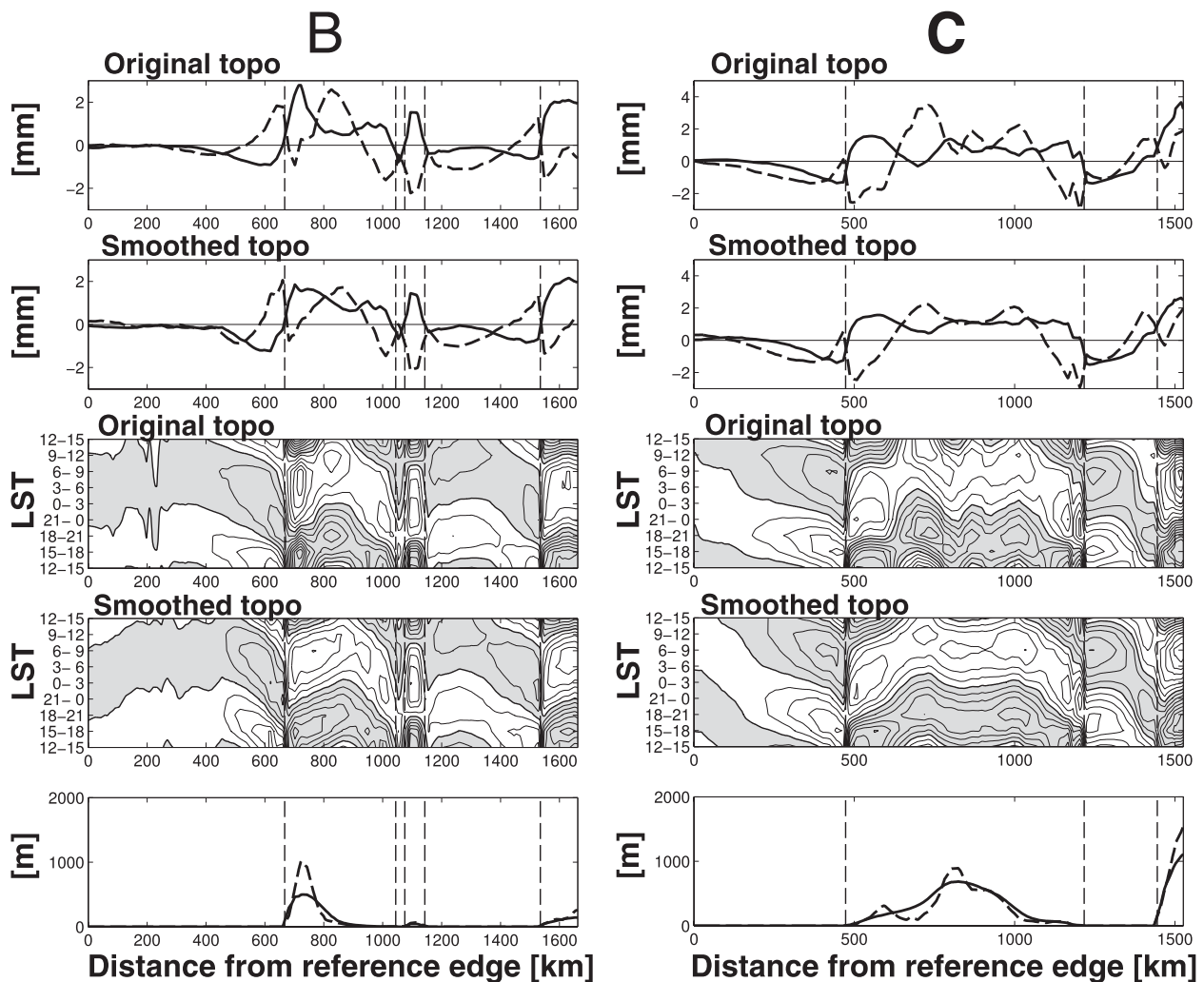
FIG. 8. As in Fig. 6 but for WRF experiments with the original and smoothed topography (shown respectively as dashed and solid lines in the bottom two panels) for transects B and C of Fig. 1. See the caption for Fig. 6 for details.

Although the second EOF shows that WRF is able to reproduce some of the local nocturnal rain features like those inland of Borneo, the propagating rain features inland and across the coastal interfaces are too slow and are limited in their extent within the model. These shortcomings are likely due to deficiencies within the convective parameterization schemes in representing the cold pool dynamics and the coupling of the local circulation with convection.

A phase lead of both modeled PC1 and PC2 compared to the observed exists, with a value of about 3 h using the 3B42 dataset or 1–2 h using the 3G68 dataset. Inadequate representation of the transition from shallow to deep convection by the convective parameterization within WRF is a possible reason.

The spatial features in the first two EOFs are mostly robust whether the 3B42 or 3G68 dataset is used. One

notable exception is in the coastal sea off north Borneo where the EOF2 for 3G68 is in closer agreement with the modeled EOF2. Such few nonrobust features are not considered in this work.

Hovmoeller analysis of the reconstructed 3B42 diurnal rain signal from the first two EOFs indicates that mountain ridges and coastlines in the Maritime Continent are sources of propagating diurnal rain signals. The complexity of the diurnal rain cycle is a consequence of the juxtaposition of coastlines and mountain ridges, causing propagating signals to interfere with one another. The stationary diurnal rain cycles over the Straits of Malacca, the Malay Peninsula, and north Sumatra are cases in point as they behave like GFD wave cavities trapping the otherwise propagating signals from the coastlines. The propagating signals travel down mountain slopes, across plains, or out into open sea, and sometimes

even cross narrow sea and penetrate distal coastal land (e.g., from west Sulawesi coast across into east Borneo). The phase speeds of propagating rain signals are found to be larger over sea than land possibly because of lower surface roughness and hence surface heat exchange over sea.

The spatial phase relation between EOF1 and EOF2 governs whether the rain signals are propagating or stationary: when the EOFs are in spatial quadrature, propagating signals result; when they are in phase or antiphase, stationary signals result. The cross sections showing simultaneously EOF1 and EOF2, for example, in Fig. 6, are helpful in understanding the propagating/stationary nature of the diurnal rain signals and the formation of GFD wave cavities.

Hovmoeller analysis of the reconstructed rainfall from WRF highlighted oversensitivity of the model to the presence of small islands and small-scale topography, generating high wavenumber components in EOF1 and EOF2. The Hovmoeller plots across various representative sections in the Maritime Continent show unrealistic disruption of propagating rain signals on the sea by small islands and of stationary rain signals inland by mountainous terrain. The lack of subgrid complexity in coastline representation and the discontinuity in model surface parameterization over land and sea may have led to sharp transition of the EOFs across model land–sea boundaries and the failure of rain features to propagate smoothly from coastal land to sea. The phase speed of propagation over open sea are correct but that over land seems too slow.

Finally, it should be noted that the observed diurnal features discussed are robust: the first two EOFs from using 10-year-averaged diurnal rain from 3B42 (not shown) are similar to those described in this work.

APPENDIX A

Phase Speed with Respect to LST

The local solar time t' for a location at a distance x east of a reference point P on the equator is related to the UTC t as follows:

$$t' = t + \frac{x}{v} + t_0, \qquad (A1)$$

where t_0 is a constant and v is the speed of the earth's rotation at the equator.

The phase of a sinusoidal wave propagating at an angle θ with the equator is

$$\phi = k'(r - c't'), \qquad (A2)$$

where r is the displacement in the direction of propagation from the reference point P, and k' and c' are, respectively, the wavenumber and phase velocity at the equator in LST coordinate.

Substituting (A1) into (A2) and noting that $x = r \cos\theta$, the phase velocity at the equator in UTC coordinate is

$$c = \left(\frac{\partial r}{\partial t}\right)_\phi = c'\left(1 - \frac{c'}{v}\cos\theta\right)^{-1}. \qquad (A3)$$

For $v \gg |c'|$,

$$c \approx c'\left(1 + \frac{c'}{v}\cos\theta\right). \qquad (A4)$$

For the rain peak propagations discussed in the text, $|c'| \sim 5$ m s^{-1} while $v \approx 460$ m s^{-1}. Hence Eq. (A4) shows that correction factor is $O(1\%)$.

APPENDIX B

Phase Relation between Principal Components of Traveling and Stationary Signals

The propagating nature of the rain signal where the EOFs are in spatial quadrature can be intuited by studying a propagating sinusoidal wave with amplitude A, wavenumber k, and frequency ω,

$$f(x,t) = A\sin(kx + \omega t). \qquad (B1)$$

Equation (B1) can be rewritten as a superposition of two standing waves:

$$f(x,t) = A\sin(kx)\cos(\omega t) + A\cos(kx)\sin(\omega t). \qquad (B2)$$

The two terms $A\sin(kx)$ and $A\cos(kx)$ in Eq. (B2) are in spatial quadrature and can be regarded as analogous to the EOFs. The terms $\cos(\omega t)$ and $\sin(\omega t)$ are in temporal quadrature and can be associated with the normalized PCS. Propagation requires that the amplitude of the two EOFs in quadrature to be equal. For the model and observed rainfall in regions where the propagating signals are identified (Fig. 6), the spatial loading of the two EOFs are about the same too.

For x increasing eastward, Eq. (B1) represents a westward-propagating wave for positive k and ω. In this case, the second PCS, $\sin(\omega t)$, lags behind the first PCS, $\cos(\omega t)$, in time while the second EOF, $\cos(kx)$, is

displaced westward of the first EOF, sin(kx). In other words, the EOF corresponding to the PCS lagging in time would be displaced in the direction of propagation when compared with the EOF corresponding to the PCS leading in time.

When the EOFs are either in phase or antiphase and the PCs have a quadrature relation, a standing wave results:

$$g(x,t) = A\sin(kx)\cos(\omega t) \pm A\sin(kx)\sin(\omega t)$$
$$= A\sqrt{2}\,\sin(kx)\cos\left(\omega t \mp \frac{\pi}{4}\right). \qquad \text{(B3)}$$

REFERENCES

Bechtold, P., J. P. Chaboureau, A. Beljaars, A. K. Betts, M. Köhler, M. Miller, and J. L. Redelsperger, 2004: The simulation of the diurnal cycle of convective precipitation over land in a global model. *Quart. J. Roy. Meteor. Soc.,* **130,** 3119–3137.

Chaboureau, J. P., F. Guichard, J. L. Redelsperger, and J. P. Lafore, 2004: The role of stability and moisture in the diurnal cycle of convection over land. *Quart. J. Roy. Meteor. Soc.,* **130,** 3105–3117.

Clark, A. J., W. A. Gallus, and T.-C. Chen, 2007: Comparison of the diurnal precipitation cycle in convection-resolving and nonconvection-resolving mesoscale models. *Mon. Wea. Rev.,* **135,** 3456–3473.

Dai, A., 2001: Global precipitation and thunderstorm frequencies. Part II: Diurnal variations. *J. Climate,* **14,** 1112–1128.

——, 2006: Precipitation characteristics in eighteen coupled climate models. *J. Climate,* **19,** 4605–4630.

Davis, C. A., K. W. Manning, R. E. Carbone, S. B. Trier, and J. D. Tuttle, 2003: Coherence of warm-season continental rainfall in numerical weather prediction models. *Mon. Wea. Rev.,* **131,** 2667–2679.

Fujita, M., F. Kimura, and M. Yoshizaki, 2010: Morning precipitation peak over the Strait of Malacca under a calm condition. *Mon. Wea. Rev.,* **138,** 1474–1486.

Guichard, F., and Coauthors, 2004: Modelling the diurnal cycle of deep precipitating convection over land with cloud-resolving models and single-column models. *Quart. J. Roy. Meteor. Soc.,* **130,** 3139–3172.

Haddad, Z. S., E. A. Smith, C. D. Kummerow, T. Iguchi, M. R. Farrar, S. L. Durden, M. Alves, and W. S. Olson, 1997: The TRMM 'day-1' radar/radiometer combined rain-profiling algorithm. *J. Meteor. Soc. Japan,* **75,** 799–809.

Hara, M., T. Yoshikane, H. G. Takahashi, F. Kimura, A. Noda, and T. Tokioka, 2009: Assessment of the diurnal cycle of precipitation over the Maritime Continent simulated by a 20 km mesh GCM using TRMM PR data. *J. Meteor. Soc. Japan,* **87,** 413–424.

Hatcher, L., A. J. Hogg, and A. W. Woods, 2000: The effects of drag on turbulent gravity currents. *J. Fluid Mech.,* **416,** 297–314.

Hsu, H.-H., and M.-Y. Lee, 2005: Topographic effects on the eastward propagation and initiation of the Madden–Julian oscillation. *J. Climate,* **18,** 795–809.

Huffman, G. J., and Coauthors, 2007: The TRMM multisatellite precipitation analysis (TMPA): Quasi-global, multiyear, combined-sensor precipitation estimates at fine scales. *J. Hydrometeor.,* **8,** 38–55.

Ichikawa, H., and T. Yasunari, 2006: Time–space characteristics of diurnal rainfall over Borneo and surrounding oceans as observed by TRMM-PR. *J. Climate,* **19,** 1238–1260.

——, and ——, 2008: Intraseasonal variability in diurnal rainfall over New Guinea and the surrounding oceans during austral summer. *J. Climate,* **21,** 2852–2868.

Jackson, J. E., 1991: *A User's Guide to Principal Components.* John Wiley and Sons, 569 pp.

Joseph, B., B. C. Bhatt, T. Y. Koh, and S. Chen, 2008: Sea breeze simulation over the Malay Peninsula in an intermonsoon period. *J. Geophys. Res.,* **113,** D20122, doi:10.1029/2008JD010319.

Kain, J. S., and J. M. Fritsch, 1990: A one-dimensional entraining/detraining plume model and its application in convective parameterization. *J. Atmos. Sci.,* **47,** 2784–2802.

——, and ——, 1993: Convective parameterization for mesoscale models: The Kain–Fritsch scheme. *The Representation of Cumulus Convection in Numerical Models, Meteor. Monogr.,* No. 24, Amer. Meteor. Soc., 165–170.

Kikuchi, K., and B. Wang, 2008: Diurnal precipitation regimes in the global tropics. *J. Climate,* **21,** 2680–2696.

Koo, M.-S., and S.-Y. Hong, 2010: Diurnal variations of simulated precipitation over East Asia in two regional climate models. *J. Geophys. Res.,* **115,** D05105, doi:10.1029/2009JD012574.

Lee, M.-I., and Coauthors, 2007a: An analysis of the warm-season diurnal cycle over the continental United States and northern Mexico in general circulation models. *J. Hydrometeor.,* **8,** 344–366.

——, and Coauthors, 2007b: Sensitivity to horizontal resolution in the AGCM simulations of warm season diurnal cycle of precipitation over the United States and northern Mexico. *J. Climate,* **20,** 1862–1881.

Mapes, B. E., T. T. Warner, and M. Xu, 2003: Diurnal patterns of rainfall in northwestern South America. Part III: Diurnal gravity waves and nocturnal convection offshore. *Mon. Wea. Rev.,* **131,** 830–844.

Mori, S., H. Jun-Ichi, Y. I. Tauhid, and M. D. Yamanaka, 2004: Diurnal land–sea rainfall peak migration over Sumatera Island, Indonesian maritime continent, observed by TRMM satellite and intensive rawinsonde soundings. *Mon. Wea. Rev.,* **132,** 2021–2039.

Neale, R., and J. Slingo, 2003: The Maritime Continent and its role in the global climate: A GCM study. *J. Climate,* **16,** 834–848.

Negri, A. J., T. L. Bell, and L. Xu, 2002: Sampling of the diurnal cycle of precipitation using TRMM. *J. Atmos. Oceanic Technol.,* **19,** 1333–1344.

Noh, Y., W. G. Cheon, S. Y. Hong, and S. Raasch, 2003: Improvement of the K-profile model for the planetary boundary layer based on large eddy simulation data. *Bound.-Layer Meteor.,* **107,** 401–427.

Oki, T., and K. Musiake, 1994: Seasonal change of the diurnal cycle of precipitation over Japan and Malaysia. *J. Appl. Meteor.,* **33,** 1445–1463.

Peng, P. T., A. Kumar, A. G. Barnston, and L. Goddard, 2000: Simulation skills of the SST-forced global climate variability of the NCEP–MRF9 and the Scripps–MPI ECHAM3 models. *J. Climate,* **13,** 3657–3679.

Qian, J. H., 2008: Why precipitation is mostly concentrated over islands in the Maritime Continent. *J. Atmos. Sci.,* **65,** 1428–1441.

——, A. Seth, and S. E. Zebiak, 2003: Reinitialized versus continuous simulations for regional climate downscaling. *Mon. Wea. Rev.,* **131,** 2857–2874.

Ramage, C. S., 1968: Role of a tropical "maritime continent" in the atmospheric circulation. *Mon. Wea. Rev.,* **96,** 365–370.

Renshaw, A. C., D. P. Rowell, and C. K. Folland, 1998: Wintertime low-frequency weather variability in the North Pacific American sector 1949–93. *J. Climate,* **11,** 1073–1093.

Ross, A. N., A. M. Tompkins, and D. J. Parker, 2004: Simple models of the role of surface fluxes in convective cold pool evolution. *J. Atmos. Sci.,* **61,** 1582–1595.

Sato, T., H. Miura, M. Satoh, Y. N. Takayabu, and Y. Wang, 2009: Diurnal cycle of precipitation in the tropics simulated in a global cloud-resolving model. *J. Climate,* **22,** 4809–4826.

Shibagaki, Y., and Coauthors, 2006: Multiscale aspects of convective systems associated with an intraseasonal oscillation over the Indonesian Maritime Continent. *Mon. Wea. Rev.,* **134,** 1682–1696.

Skamarock, W. C., and Coauthors, 2008: A description of the Advanced Research WRF version 3. NCAR Tech. Note NCAR/TN-475+STR, 113 pp. [Available online at http://www.mmm.ucar.edu/wrf/users/docs/arw_v3.pdf.]

Stauffer, D. R., and N. L. Seaman, 1990: Use of four-dimensional data assimilation in a limited-area mesoscale model. Part I: Experiments with synoptic-scale data. *Mon. Wea. Rev.,* **118,** 1250–1277.

Sui, C. H., K. M. Lau, Y. N. Takayabu, and D. A. Short, 1997: Diurnal variations in tropical oceanic cumulus convection during TOGA COARE. *J. Atmos. Sci.,* **54,** 639–655.

Tao, W. K., S. Lang, J. Simpson, C. H. Sui, B. Ferrier, and M. D. Chou, 1996: Mechanisms of cloud–radiation interaction in the tropics and midlatitudes. *J. Atmos. Sci.,* **53,** 2624–2651.

Waliser, D. E., and M. Moncrieff, 2008: The Year of Tropical Convection (YOTC) Science Plan: A joint WCRP–WWRP/THORPEX international initiative. WMO/TD 1452, WCRP–130, WWRP/THORPEX 9, 26 pp. [Available online at http://www.ucar.edu/yotc/documents/YOTC_Science_Plan.pdf.]

Wang, S.-Y., R. R. Gillies, E. S. Takle, and W. J. Gutowski Jr., 2009: Evaluation of precipitation in the Intermountain Region as simulated by the NARCCAP regional climate models. *Geophys. Res. Lett.,* **36,** L11704, doi:10.1029/2009GL037930.

Wang, Y., L. Zhou, and K. Hamilton, 2007: Effect of convective entrainment/detrainment on the simulation of the tropical precipitation diurnal cycle. *Mon. Wea. Rev.,* **135,** 567–585.

Wu, C.-H., and H.-H. Hsu, 2009: Topographic influence on the MJO in the Maritime Continent. *J. Climate,* **22,** 5433–5448.

Wu, P. M., M. Hara, H. Fudeyasu, M. D. Yamanaka, J. Matsumoto, F. Syamsudin, R. Sulistyowati, and Y. S. Djajadihardja, 2007: The impact of trans-equatorial monsoon flow on the formation of repeated torrential rains over Java Island. *SOLA,* **3,** 93–96.

——, M. D. Yamanaka, and J. Matsumoto, 2008: The formation of nocturnal rainfall offshore from convection over western Kalimantan (Borneo) Island. *J. Meteor. Soc. Japan,* **86,** 187–203.

——, J.-I. Hamada, M. D. Yamanaka, J. Matsumoto, and M. Hara, 2009a: The impact of orographically-induced gravity wave on the diurnal cycle of rainfall over southeast Kalimantan Island. *Atmos. Oceanic Sci. Lett.,* **2,** 35–39.

——, M. Hara, J.-I. Hamada, M. D. Yamanaka, and F. Kimura, 2009b: Why a large amount of rain falls over the sea in the vicinity of western Sumatra Island during nighttime. *J. Appl. Meteor. Climatol.,* **48,** 1345–1361.

Yang, G. Y., and J. Slingo, 2001: The diurnal cycle in the tropics. *Mon. Wea. Rev.,* **129,** 784–801.

Zhou, L., and Y. Q. Wang, 2006: Tropical Rainfall Measuring Mission observation and regional model study of precipitation diurnal cycle in the New Guinean region. *J. Geophys. Res.,* **111,** D17104, doi:10.1029/2006JD007243.

Zhou, T., R. Yu, H. Chen, A. Dai, and Y. Pan, 2008: Summer precipitation frequency, intensity, and diurnal cycle over China: A comparison of satellite data with rain gauge observations. *J. Climate,* **21,** 3997–4010.